Continuous water adsorption states promoted by Ni^{2+} confined in a smectite

M. A. S. Altoé[1,2], L. Michels[2,*], E. C. dos Santos[2,3], R. Droppa Jr[3], G. Grassi[1], L. Ribeiro[5], K.D. Knudsen[6,2], H. N. Bordallo[3,7], J. O. Fossum[2,*], G. J. da Silva[1]

[1]Instituto de Física, Universidade de Brasília, 70.919-970, Brasília – DF, Brasil

[2]Department of Physics, Norwegian University of Science and Technology – NO-7495, Trondheim, Norway

[3]Niels Bohr Institute, University of Copenhagen, 2100, Copenhagen, Denmark

[4]Centro de Ciências Naturais e Humanas, Universidade Federal do ABC, 09.210-580, Santo André – SP, Brasil

[5]Unidade Universitária de Ciências Exatas e Tecnológicas, Universidade Estadual de Goiás, 75.132-903, Anápolis– GO, Brasil

[6]Physics Department, Institute for Energy Technology, IFE, Kjeller, Norway

[7]European Spallation Source, Tunavägen 24, 22100, Lund, Sweden

*Correspondences: leander.michels@ntnu.no

jon.fossum@ntnu.no

Abstract:

The water adsorptions isotherms of the smectite Ni-fluorohectorite have been obtained from the relative humidity dependence of X-ray diffraction intensities, and it was observed that the transitions between the stable hydration states are continuous; a behavior which is markedly different from previous studies of Na-fluorohectorite and Li-fluorohectorite smectite. It was also observed that the environmental history of the clay samples is important for the detailed behavior displayed by these isotherms. In addition, based on thermogravimetric and differential scanning calorimetry measurements, a complete Ni-fluorohectorite dehydrated state only can be reached at long (several hours) isotherm times at 70 °C, or at shorter times (minutes) above 150 °C. Our observations are consistent with the existence of various forms of Ni^{2+}-H$_2$O complexes in Ni-fluorohectorite, and we suggest that the present observations can be extended to other smectites with transition metals as interlayer charge compensating cations, and consequently have significant practical consequences in materials science and other areas where smectite clays are important.

Graphical Abstract:
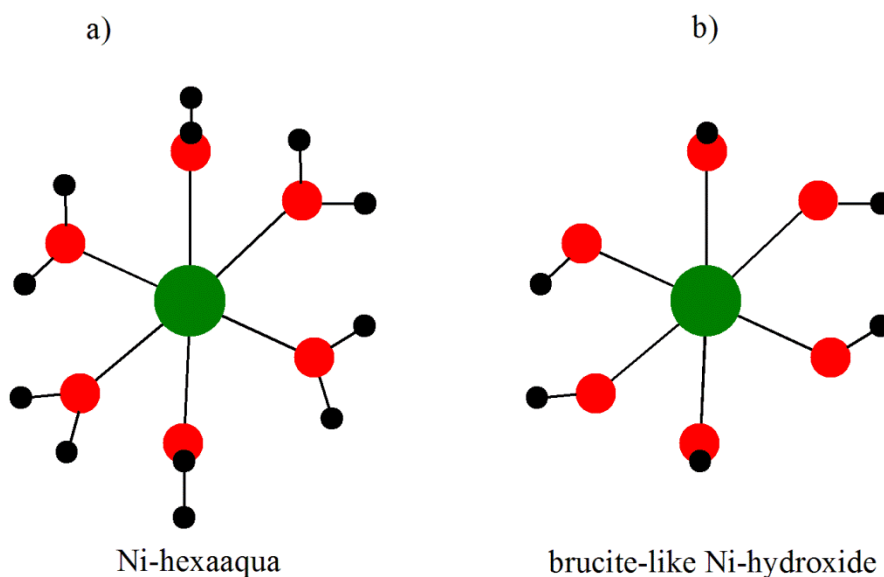
a) Hydration structure of Ni^{2+} hexaaqua, which occurs for high RH conditions. b) Structure of Ni-brucite.

Introduction

Smectites or clay minerals are among the most abundant minerals on Earth and are rarely found in nature without intercalated H_2O. The large scientific and technological interest in smectites is connected to their ability to swell, most commonly caused by their interactions with H_2O.(Sposito et al., 1999) Therefore whether smectites are used for, CO_2,(Giesting et al., 2012a; Michels et al., 2015; Schaef et al., 2012) capture, nuclear waste storage(Sellin and Leupin, 2013), heavy metal removal(Oueslati et al., 2011) or for drug delivery(Aguzzi et al., 2014), understanding their interactions with H_2O is of paramount importance.

Smectite contain charge-compensating cations in their nano-sized quasi 2-dimensional interlayers (pore width less than 2 nm). These cations balance the negative surface charge of the smectite sheets, and as a whole this system is responsible for the well-known swelling dynamics (Bordallo et al., 2008). Either crystalline (intercalation), or osmotic (exfoliation) swelling occurs when clay particles interact with foreign molecules, such as H_2O (Hansen et al., 2012; Tenorio et al., 2010) or CO_2 (Giesting et al., 2012b; Hemmen et al., 2012) The variation of the basal spacing of hydrated smectites is connected primarily to the number of H_2O molecules intercalated within the layers, and equilibration at different relative humidity and temperatures. The H_2O molecules may be arranged within the smectite interlayer space in structures corresponding to integral number of water layers (WL) (Ferrage et al., 2010; Tamura et al., 2000) or more complex H_2O structures (Morrow et al., 2013; Tenorio et al., 2010). In order to study this crystalline swelling process many methods have been employed, such as quasi-elastic neutron scattering (QENS) (Gates et al., 2012; Malikova et al., 2007; Malikova et al., 2006; Mitra et al., 2013), Neutron Diffraction (Hawkins and Egelstaff, 1980; Skipper et al., 1994; Zhou et al., 2015), X-ray diffraction (XRD) (da Silva et al., 2002; Dazas et al.,

2013; Ferrage et al., 2010; Ferrage et al., 2005; Ferrage et al., 2011; Oueslati et al., 2011; Tenorio et al., 2008; Tenorio et al., 2010), NMR (Fleury et al., 2013; Tenorio et al., 2008; Tenorio et al., 2010) and molecular dynamics simulations (Ebrahimi et al., 2014; Skipper et al., 1991a; Tambach et al., 2004; Zheng and Zaoui, 2011).

Synthetic clay minerals have the advantage that they possess a more homogeneous charge distribution, and also contain significantly fewer impurities (e.g. carbonates, (hydr)oxides, silica, and organic matter) than their natural counterparts (Bergaya and Lagaly, 2013). Fluorohectorites (Fh) have often been used as a representative and clean model system of natural smectite clays (Ayyappan et al., 1996; da Silva et al., 2003; Dazas et al., 2013; Hansen et al., 2012; Hemmen et al., 2010; Malikova et al., 2007; Tenorio et al., 2010). Hectorite is a 2:1 phyllosilicate, meaning that the layers are formed by two inverted silicate tetrahedral sheets, sharing their apical oxygen with one octahedral sheet sandwiched in between and it is classified as a trioctahedral smectite since Li^+ substitutes for Mg^{2+} in the octahedral sheet sites, which are fully occupied. The proportion x of the Li^+ ions in the clay sheet structure itself determines the surface charge of the layers, which are held together in the stacked structure by sharing the interlayer cation.

Considering that the type of intercalated cation substantially influences the physicochemical behaviors of the system (Chatterjee et al., 2004), the present work investigates the effects of intercalating Fh with the divalent cation Ni^{2+}, hereafter termed NiFh clay. Ni-intercalated cations in smectites have been extensively studied by the scientific community (Grassi et al., 2014; Michels et al., 2014; Oueslati et al., 2011; Pascual et al., 2014; Pitteloud et al., 2001; Skipper et al., 1991b; Zheng and Zaoui, 2011; Zheng et al., 2010), partly motivated by substantial increase of the amounts of heavy metals in the environment. Our interest in NiFh is also partly based in the well-known fact that Ni^{2+} and water in basic pH conditions form a Ni-hydroxide (Ni-brucite) structure, with chemical formula $Ni(OH)_2$, and that the Ni-brucite structure coexist with the NiFh particles(Michels et al., 2014). Therefore new features related to simultaneous NiFh-water and the Ni-brucite-water interactions could be expected, and our aim in the present work is to investigate and understand the origin of such features.

We here report on two different types of X-ray diffraction (XRD) experiments that were performed on NiFh powder. The first type consisted in mapping small interlayer displacements measured from the (001) Bragg peak positions as a function of relative humidity (RH) at two different fixed temperatures. In the second type of XRD experiment, the particle thickness and the lattice strain were calculated using the standard Williamson-Hall analysis method, based on the evolution of the (001) as well as higher order Bragg peaks measured at selected values of RH. In addition, thermal analysis was performed, demonstrating that NiFh clay shows a quite distinct behavior compared to that observed in other smectites upon water adsorption. We explore this in detail and suggest possible explanations for these behaviors.

1. Materials and Methods

1.1 Sample Preparation

The Ni-fluorohectorite (NiFh) samples were obtained by a cation exchange protocol starting from Li-Fluorohectorite (LiFh), described by our group previously (Grassi et al., 2014; Michels et al., 2014). This consists in mixing LiFh and $NiCl_2 \cdot 6H_2O$ in a water solution and collecting the powder after centrifuging. The NiFh powder is then washed in deionized water several times in order to remove residual salt. The nominal chemical formula of the product thus obtained is $Ni_{0.6} - \left[Mg_{(4.8)} Li_{1.2} \right] Si_8 O_{20} F_4$ per unit cell. The pH was measured to be 9.5 during the cation exchange process, as adjusted by the clay dispersion itself. The samples are left to dry and after evaporation of the water, the sedimented film is collected and placed in the sample chamber described in Figure 1. Previous to the XRD analyses, two kinds of samples were prepared from the pristine NiFh:

A. Non-preheated NiFh: Two samples of clay mineral with the same initial relative humidity (RH) were placed under N_2 atmosphere and their structural change was monitored in-situ using XRD, at two different temperatures: one at 70 °C and another at 20 °C, without prior preheating of the samples.

B. Pre-heated NiFh: Two samples of clay minerals were placed on a heater plate and pre-heated at 150 °C under N_2 atmosphere until their dehydrated structure was obtained, which was monitored in-situ using XRD. After dehydration, the temperature of one sample was lowered to 70 °C and a number of XRD patterns were collected for various values of RH, as detailed below. In addition, this same procedure was repeated with the other set of pre-heated NiFh at 20 °C.

After the sample preparation described above, the treated NiFh powder was placed inside a sample cell, in which RH and temperature could be accurately controlled. This custom made cell consists of a closed cylindrical chamber with a small kapton window for XRD transmission, a heater plate as sample holder in the center and a humidity/temperature sensor inside. The RH was controlled by regulating a pure nitrogen (N_2) flux into the chamber. The N_2 gas was separated into two branches: one going into a water container, where N_2 was saturated with water vapor, and the other conducting the dry N_2 gas to the chamber. Both channels had flow meters installed in their respective flow paths for reproducibility control of the applied RH. This apparatus allows for mixing humid and dry gases in a controlled manner. A sketch of this experimental setup is shown in Figure 1.

122
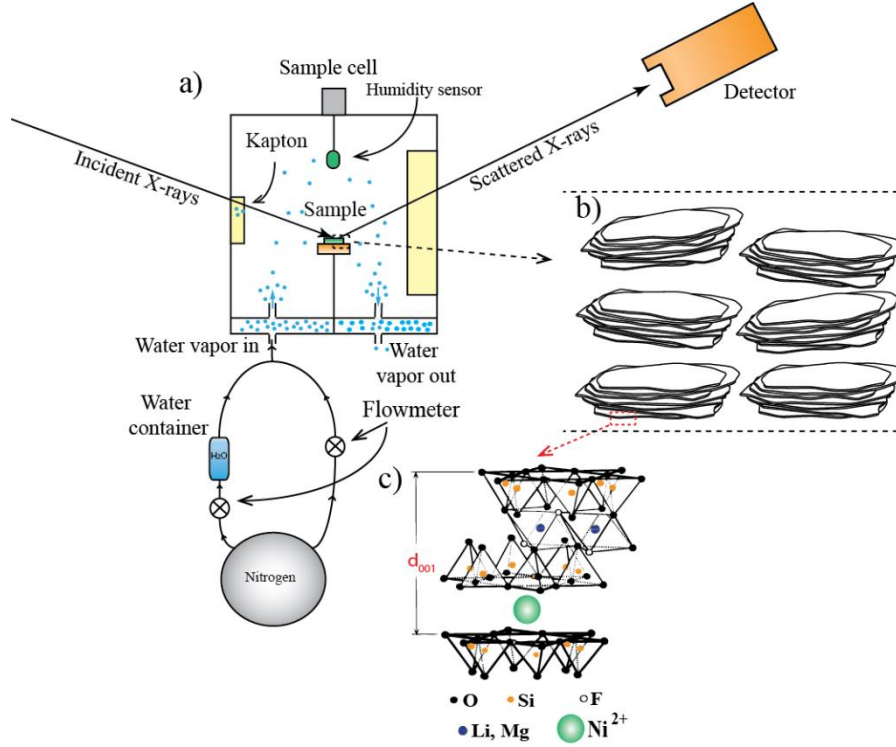
123   **Figure 1:** a) Schematics of the sample cell which consists of a heater plate, kept inside a closed cylindrical

124   sample chamber together with a humidity/temperature sensor. b) Aligned sedimented film of smectite clay

125   mineral particles. c) The layer structure of the fluorohectorite with the charge compensating cation Ni^{2+} confined

126   in the unit cell interlayer space (d_{001}).

1.2 XRD Experiments

XRD measurements on non-preheated samples were studied using an in-house (NTNU, Trondheim) Bruker NanoSTAR X-ray scattering instrument, attached to a Xenocs X-ray source with a copper anode. Preheated samples were measured at the Brazilian Synchrotron Light Source Laboratory (LNLS) at the XRD2 beam line, using a wavelength of $\lambda = 0.154991$ nm.

The scattered X-ray intensities are plotted in terms of the scattering vector defined as $q = 4\pi sin(\theta)/\lambda$, where 2θ is the scattering angle. In order to obtain the peak positions and de-convolute the peak widths, which are intrinsic to the sample, a pseudo-Voigt peak shape function was used. For our purpose this function provides a good approximation to the convolution of Lorentzian and Gaussian functions(Wertheim et al., 1974):

$$\Phi(q) = \mu \frac{2}{\pi} \frac{\Gamma}{4(q-q_c)^2 + \Gamma^2} + (1-\mu)\frac{\sqrt{4\ln 2}}{\sqrt{\pi}\Gamma}\exp\left[\frac{-4\ln 2(q-q_c)^2}{\Gamma}\right] \tag{1}$$

μ is the proportional constant that ranges from zero to one and it is responsible for peak shape curve being more Lorentzian or Gaussian while Γ denotes the experimental peak width of curves.

5

140
$$\mu = 1.36603\left(\frac{\omega_L}{\Gamma}\right) - 0.47719\left(\frac{\omega_L}{\Gamma}\right)^2 + 0.11116\left(\frac{\omega_L}{\Gamma}\right)^3$$

$$\Gamma = \left(\omega_G^5 + 2.69269\omega_G^4\omega_L + 2.42843\omega_G^3\omega_L^2 + 4.47163\omega_G^2\omega_L^3 + 0.07842\omega_G\omega_L^4 + \omega_L^5\right)^{1/5}$$

141     $\Phi(q)$ is the interference function related to the measured intensity by $I(q) = C(q)\Phi(q)$. The $C(q)$

142   parameter is related to the scattering structure factor and to the Lorentz-polarization factor, and in the

143   region around each (00ℓ) peak, $C(q)$ can be approximated by a constant since its value fall steeply at

144   low q and varies slowly with q in the range of the peak widths. The ω_L and ω_G denotes the peak

145   widths of the Lorentzian and Gaussian components that represent the sample and instrumental

146   contribution to the line broadening respectively. At NTNU the FWHM Gaussian instrumental

147   resolution width, obtained from the fittings, was $\omega_G \approx 0.196 \pm 0.005$ nm^{-1} (Cases of Figures 2 (b) and

148   (d) below), and at LNLS it was $\omega_G \approx 0.043 \pm 0.009$ nm^{-1} (Cases of Figures 2 (a), (c) and Fig. 3

149   below).

150   Only for the Williamson-Hall procedure (Case of Figures 5 and 6 below) a Ge (111) single crystal

151   analyzer was utilized at LNLS in front of the diffracted X-ray beam detector in order to sharpen the

152   instrumental resolution, thus reducing the effects of instrumental broadening on the diffractograms but

153   also reducing significantly the XRD intensity. This setup allows the data to be fitted with only a

154   Lorentzian i.e. the instrumental width contribution can be neglected, and the pseudo-Voigt function is

155   not needed.

156   *1.3 Thermogravimetric Analysis*

157   Thermal gravimetric analysis (TGA) and Differential Scanning Calorimetry (DSC) measurements

158   were performed using respectively a TG 209 F1 LIBRA and a DSC 214 Polyma from NETZSCH.

159   The experimental conditions were: N_2 atmosphere $\approx$ (40 ml/min), heating rate (10 °C.min^{-1}), platinum

160   top-opened crucible (TGA) and aluminum pierced crucible (DSC). The samples weights were approx.

161   20 mg. The results allowed quantifying the amount of initial H_2O in the clays layers as well as to

162   describe the different phases as follows. Two types of measurements were performed using the TGA:

163   one to measure the mass loss as a function of temperature carried out between 25 °C to 400 °C and the

164   other to observe the evolution of the mass loss at constant temperature. The former can give the

165   temperature where the H_2O populations de-adsorb from the sample, while in the latter (by fixing the

166   temperature at 70 °C and 150 °C) one can determine the mass loss as a function of time.

167   Consequently, the isotherm method allows us to directly compare the relation between the initial H_2O

168   content and the XRD Bragg peak position. On the other hand, the differential scanning calorimetry

169   (DSC) measurements, performed between room temperature and 400 °C, allows to quantify the H_2O

170   transitions in the samples.

2.   Results

A. XRD: It is well-known that smectite clays at finite values of RH expand (swell) in the z-direction (00ℓ). Therefore, the peak positions q_c, obtained from Eq. (1), for a given RH are related to the hydration state, which depends on the type of interlayer cation. As reported in several previous publications(da Silva et al., 2002; Ferrage et al., 2010; Ferrage et al., 2005; Ferrage et al., 2011; Gates et al., 2012), for Na$^+$ the stable hydration states correspond to zero water layer (0WL) (dehydrated peak), one water layer (1WL) and two water layers (2WL). For the case of Li$^+$ as interlayer cation(Tenorio et al., 2010), the stable hydration states are 0WL, 1WL, one-and-a-half WL (1.5 WL) and 2WL.
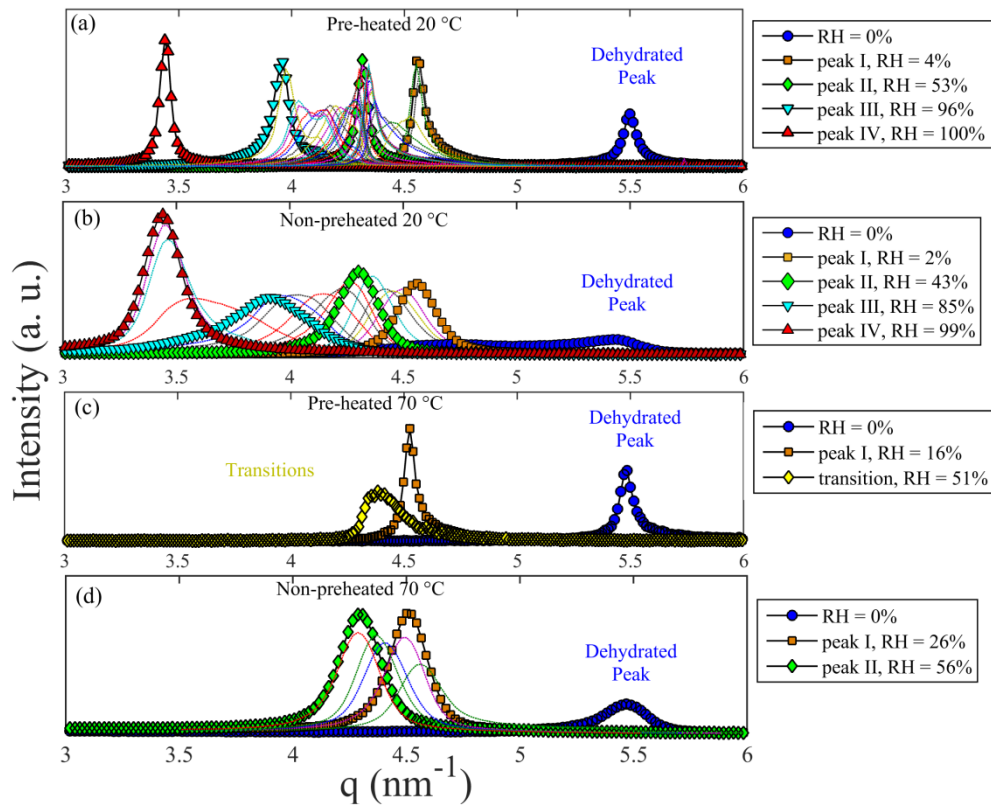
Figure 2: The diffraction peaks corresponding to the stable hydration states (see Figure 3) in NiFh with the corresponding RH for a sample that is (a) pre-heated T = 20 °C, (b) non-pre-heated T = 20 °C, (c) pre-heated T = 70 °C and (d) non-pre-heated 70 °C. The thin continuous lines represent transition states in between the stable hydration states (i.e. peaks I, II, III and IV). The non-preheated samples measured at NTNU have broader peak widths due to the instrumental contribution as explained in the text.

In this work, the expansion for NiFh was carefully followed by monitoring the position of the (001) Bragg peak for increasing values of RH. Figure 2 shows the Bragg peak position as a function of q for different values of RH. The value of d_{001}, i. e., the distance between the basal planes, was then calculated using the relation:

$$190 \qquad\qquad\qquad\qquad q_c = \frac{2\pi}{d_{001}} \qquad\qquad\qquad\qquad (2)$$

191   The peak at $q_c \approx 5.5$ nm^{-1} (blue ○) found in all diagrams, represent the dehydrated condition

192   corresponding to basal distance $d_{001} = 1.14$ nm, implying that there is not enough space between the

193   clay layers to accommodate H_2O molecules. The other peaks, hereafter denoted as peak I to peak IV,

194   correspond to the conditions where the H_2O intercalates into the interlayer space

195   For the pre-heated and non-pre-heated samples measured at T = 20 °C (two upper panels), the

196   peak positions in Figure. 2 are: peak I with $q_c \approx 4.55$ nm^{-1} at RH = 4%, peak II with $q_c \approx 4.31$ nm^{-1} at

197   RH = 53%, peak III with $q_c \approx 3.96$ nm^{-1} at RH 96% and finally peak IV with $q_c \approx 3.44$ nm^{-1} at RH =

198   100%. On the other hand, for samples pre-heated and non-pre-heated and measured at T = 70 °C (two

199   lower panels) the low q peaks (III and IV) are not observed. Moreover, although the peak positions

200   related to stable peaks remain the same when compared with the samples at 20 °C they are shifted to

201   different RH values. In addition, for the non-pre-heated sample measured at T = 70 °C a transition

202   from peak I to peak II is observed, while the range around peak II (green ◇) contains multiple peaks

203   for various RH values. This can be considered as a continuum of transitions between peak I (orange
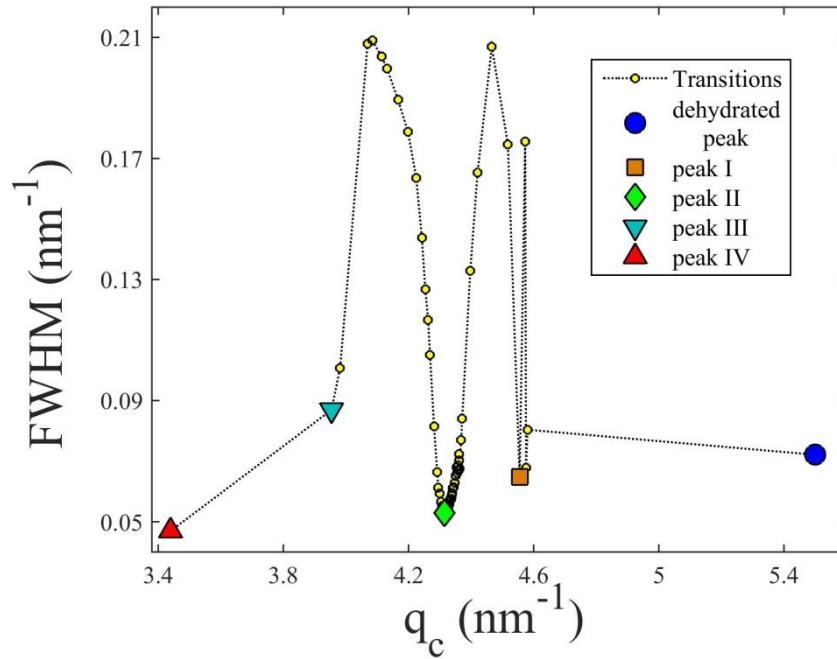
204   □) and peak III (cyan ▽).

205   In order to check whether these peaks are stable hydration states or not, a pseudo-Voigt

206   function, Eq. (1), was used to fit the diffractograms depicted in Figure 2. The resulting FWHM values,

207   ω_L, for the pre-heated sample measured at 20 °C are plotted as a function of q_c in Figure 3.

Figure 3: FWHM (ω_L) as a function of the position of the Bragg peak q_c for pre-heated sample at T = 20 °C. The stable hydration states (large symbols) show narrower FWHM compared to of the transient peaks.

It is known that the FWHM is related to the structural ordering of the crystalline material. More ordered and/or thicker structures will generally give smaller FWHM values. Therefore the peak positions, q_c, where the FWHM shows a minimum (large symbols in Figure 3) can be related to hydration states where the crystalline structure has a higher degree of ordering. This distinguishes them from the broader diffractograms of the mixed intercalated states, represented as transient states (yellow dots ○) in Figure 3.

The average diameter of a freely rotating water molecule is approximately 0.29 nm(Israelachvili, 2011). When water is present in the interlayer space of clay minerals, the d_{001} value is often related to the amount of H_2O "layers" present. For each hydration state there are intervals of corresponding d_{001}. If the d_{001} value from the dehydrated state (1.146 nm) is subtracted from the average of the stable d_{001} values, the resulting number is the effective interlayer space occupied by H_2O molecules. The results are shown in Table 1 for T = 20 °C.

Table 1: The average value of the d_{001} corresponding to each peak type (defined as I to IV in Figure 2). The value of 1.146 nm, which is the d_{001} of 0WL, is subtracted in order to calculate the amount of H_2O "layers" for stable hydration state.

Peak type	Mean d_{001} (nm)	Subtracting the 0WL (1.146 nm)	Effective number of H_2O Layers

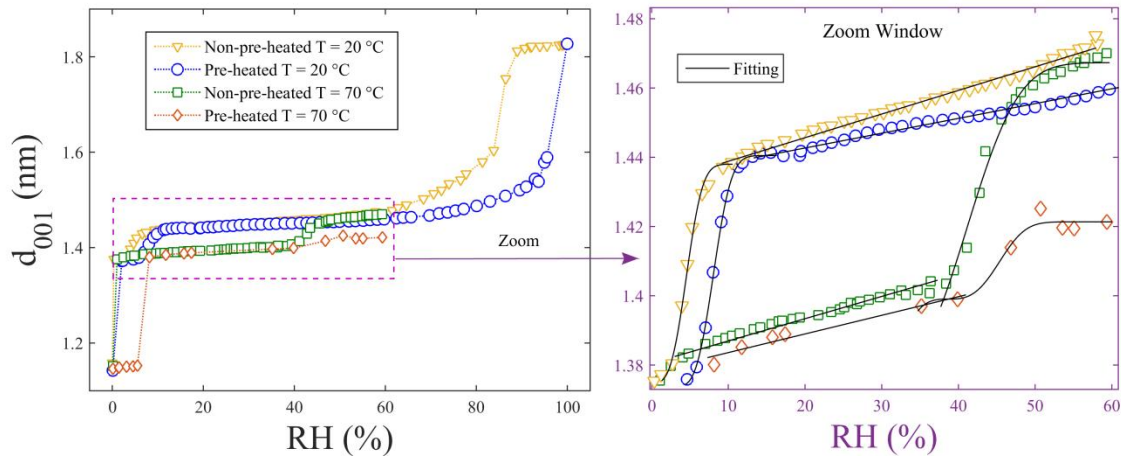|			
Peak I	1.3749 ± 0.0034	0.2289	0.80
Peak II	1.4439 ± 0.0040	0.2979	1
Peak III	1.5685 ± 0.0267	0.4225	1.5
Peak IV	1.8269	0.6809	2.3

227

228   Now we turn to the analysis of peak positions of the diffractograms in Figure 2, which can be

229   represented in terms of d_{001} stacking distances using Eq. (2), as a function of RH. The results are

230   shown in Figure 4.

231

Figure 4: Stacking distance d_{001} as function of RH. The value of d_{001} is related to the amount of H_2O within the
interlayer space. The inset shows the continuous transition from peak I to peak II. The transition from peak II to
peak III is not abrupt as is evident since d_{001} grows continuously. The zoom window (right panel) shows the fit
of an Avrami-like model (Eq. 4) to the data see description in the text. Pre-heated samples are exposed to pure
dry N_2 and heated to 150 °C until the dehydrated Bragg peak position is reached and then the temperature is
lowered to 20 °C or 70 °C. The non-pre-heated samples are dried at 20 °C or 70 °C in pure N_2 atmosphere until
the dehydrated Bragg peak position is reached (see Methods).

239   As RH increases, d_{001} increases as well. For low RH values, the transition from the dehydrated

240   state to the state containing peak I is seen to be abrupt in all cases, whilst the transition from peak I to

241   peak II displays an "*S*-shaped" change. The transition from peak II to peak III is not clearly visible,

242   instead a continuous increment of d_{001} is observed from 2% to 96% of RH until d_{001} clearly changes to

243   the peak IV position. The results indicate continuous peak shifts in the transition regions, which have

244   not been observed in previous hydration studies of synthetic smectites(Hemmen et al., 2010; Tamura

245   et al., 2000), and our results clearly differ from the abrupt stepwise expansion of the layer-to-layer

246   distance with increasing water activity normally reported for smectites(Dazas et al., 2015). The

247   change in temperature (20 or 70 °C) does not seem to affect either the continuous behavior or the

248   presence of an abrupt transition for low RH values. However, the initial sample condition clearly

249   influences the transition between peaks I and II. In the non-pre-heated case, this transition is observed

250 to be shifted to higher RH values at T = 70 °C (yellow and green curves in the right panel of Fig. 4) ,

251 whereas for the pre-heated sample at 70 °C the transition is not clearly observed.

252   For the sample pre-heated and measured at T = 20 °C (blue curve), the evolution of d_{001}, after

253 the transition from peak I to II, could be fitted with a linear function, with slope η as given by Eq. 3,

254 up to approximately RH = 60%.

$$d_{001} = \eta \cdot RH \tag{3}$$

256 In the case of the measurements performed at T = 70 °C, this linear behavior is also observed for the

257 pre-heated sample (red curve), as well as for the non-pre-heated sample below the transition from

258 peak I to peak II (green curve). In addition, the evolution of d_{001}, during the transition from peak I to

259 peak II, was found to be well described by an exponential law:

260

$$d_{I \to II} = d_{II} - (d_{II} - d_I)\exp\left[-K(RH - RH_I)^{\alpha}\right] \tag{4}$$

262 where, d_{II} is the interlayer spacing of the hydration state corresponding to peak II, d_I is the interlayer

263 spacing of the hydration state corresponding to peak I, and RH_I is the RH value at which the transition

264 begins for the increasing RH. Thus the whole range shown in the right panel of Fig. 4 could be fitted

265 with a combined equation, and the resulting parameters, represented by the continuous lines in the

266 right panel of Figure 4, are shown in Table 2.

267 Table 2: Fitting parameters obtained from Eq. (3) and (4).

| Parameters	Pre-heated T = 20 °C	Pre-heated T = 70 °C	Non-pre-heated T = 20 °C	Non-pre-heated T = 70 °C
η (slope)	$(4.3 \pm 0.2)\cdot10^{-4}$	$(4.8 \pm 0.6)\cdot10^{-4}$	$(6.8 \pm 0.2)\cdot10^{-4}$	$(6.4 \pm 0.6)\cdot10^{-4}$
d_{II}	1.4410±0.0005	1.420±0.002	1.441 ± 0.003	1.455 ± 0.004
d_I	1.373±0.001	1.399±0.002	1.375 ± 0.005	1.398 ± 0.003
RH_I	3.5 ± 0.6	38 ± 1	0 ± 1	36±1
K	$(7 \pm 1)\cdot10^{-3}$	$(2 \pm 1)\cdot10^{-3}$	$(7 \pm 5)\cdot10^{-3}$	$(2 \pm 1)\cdot10^{-3}$
α	3	3	3	3

268

269   The slope, η, obtained by fitting in the linear regime, represents how H_2O intercalates into the

270 interlayer space of NiFh in the continuous regime. Previous work performed at T = 15 °C on

271 NaFh(Hemmen et al., 2010) gave an estimated slope in the same range as those obtained here.

272 Furthermore, based on Table 2, the η values are related to the initial condition of the clays. The pre-

273 heated samples have approximately the same values of η, which are smaller than those observed for

274   the non-pre-heated samples. Thus our results indicate that the intercalation process in this region is

275   temperature independent (at least in the temperature range probed in this study), i.e. the rate of H_2O

276   intercalation (η) in the non-transition region seems to depend only on the environmental history of the

277   clays. It is clear however that the temperature (20 or 70 °C) shifts the RH value for which the

278   transition peak I → peak II occurs. This is reflected by the fitting parameter RH_I that shows that it is

279   more difficult to intercalate H_2O at higher temperatures. Similar observations were reported by da

280   Silva et al. in Na-fluorohectorite(da Silva et al., 2003).

281   The parameters α and K, defined in Eq. (3) may be discussed in terms of the Avrami

282   equation(Gasparini et al., 2013), where K represents the transition rate constant, while α is an integer

283   between 1 and 4, where $\alpha = 3$ is normally interpreted as the case of 3-dimensional nucleation growth.

284   However, while the standard Avrami model describes time dependent processes, the present case is an

285   equilibrium process. The equation can however be adapted to the present case where the cation is

286   already solvated and the water only fills the interlayer space. The fitting shows that K is independent

287   of the initial condition of the sample (pre-heated or non-pre-heated) and is higher for T = 20 °C than

288   at T = 70 °C.

289   Together, these considerations, taken with appropriate care, show that smectite clay hydration

290   can be very sensitive to initial sample preparation and environmental history. Similar conclusions

291   regarding preparation and environmental history were reported in a work on the synthetic smectite

292   laponite by Cummins et al. (Cummins, 2007). We suggest that such behaviors also may apply to other

293   of the transition metals intercalated smectites.

294   **B. Layer Thickness and Lattice Strain:** The obtained XRD peak intensities are shown in

295   Figure 5 for the pre-heated sample at T = 20 °C.
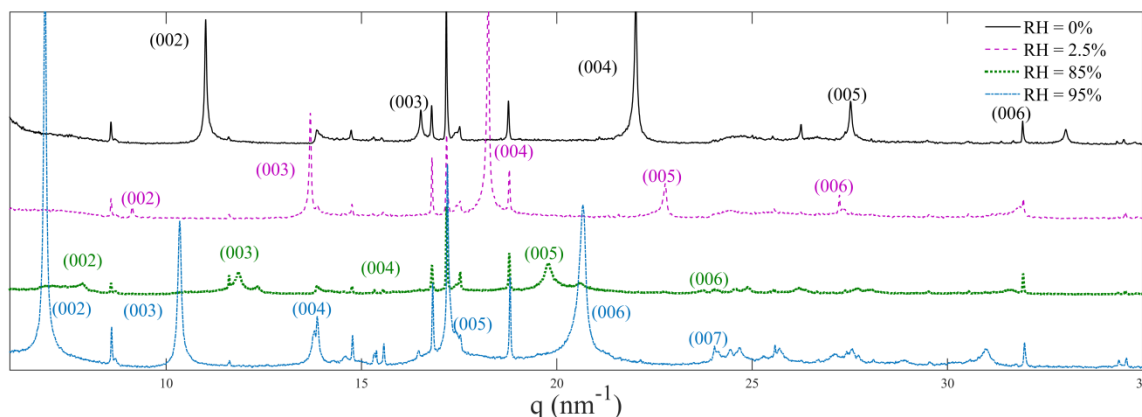
296

Figure 5: XRD (*00ℓ*) intensities of the NiFh samples at different RH. In this case, the use of crystal analyzer
makes the instrumental contribution to the line broadening negligible.

299   Considering that the contributions to the FWHM of the peaks are average thickness of the

300   clay particle stacks, plus the strain or disorder in the lattice spacing, we make use of a Williamson-

301   Hall (W-H)(da Silva et al., 2002) plot to analyze these data as follows:

$$302 \qquad\qquad \omega_L = \frac{2\pi}{Nd} + \xi q \qquad\qquad\qquad (5)$$

303　where ω_L is the FWHM obtained from the Lorentzian fitting of the XRD curves shown in Figure 5,

304　Nd is the average particle stack thickness, obtained from the extrapolation of the straight line to $q = 0$,

305　and ξ is the average lattice strain, defined as $\frac{\Delta q_c}{q_c}$, or disorder, obtained from the slope of the straight

306　line. The results of this analysis, performed for four different values of RH, are presented in Figure 6.

307
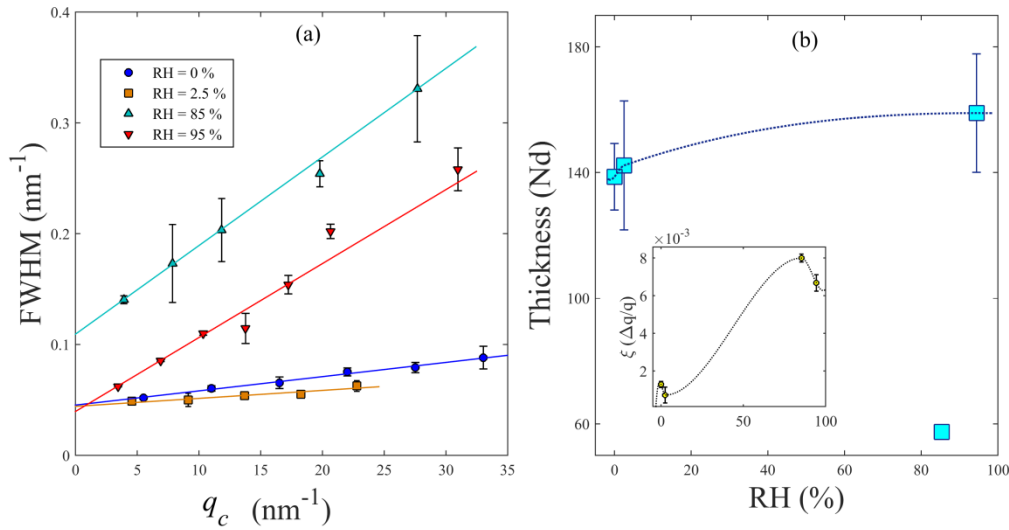
Figure 6: a) Williamson-Hall (W-H) plot, for RH values at 0%, 2.5%, 85% and 95%, with the slope and intercept giving the average strain and the average particle thickness respectively. b) The estimated particle thickness and lattice strain (inset).

311　　　Figure 6 (a) shows the W-H plots for 0%, 2.5%, 85% and 95% of RH for pre-heated samples

312　studied at T = 20 °C, from which both the average particle thickness and lattice strain were extracted

313　and presented in Figure 6 (b). The particle thickness, $Nd = 146 \pm 11$, shown Figure 6 (b), remains

314　approximately constant for 0%, 2.5%, 95% of RH. The exception is the case of RH = 85 %, where

315　low particle thickness value may be attributed to the fact that at this condition the sample is in a

316　transition between the regions of the peak II to peak III (as shown in Figure 4). In this case, the

317　intercalated H_2O might not occupy the clay interlayers homogeneously, resulting in an increase of the

318　lattice strain (see inset) and thus affecting the stability. The minimum strain, at low RH values, can be

319　interpreted as a condition where the clay NiFh has its basal planes more ordered in the stacking layers,

320　i.e. closer to each other due to the lack of intercalated H_2O. On the other hand, an increase of H_2O

321　(higher humidity) disassociates the basal planes from each other allowing for more freedom and thus

322　possibly a more disordered (higher lattice strain) layered orientation.

323 **C. TGA and DSC:** The H_2O adsorbed differentially in the sample can be identified by
324 measuring the mass loss as function of temperature. Figure 7 (a) shows the mass loss of both NiFh
325 and Ni-brucite as function of temperature and Figure 7(b) the quantifications of the H_2O transitions
326 within the clay particles.
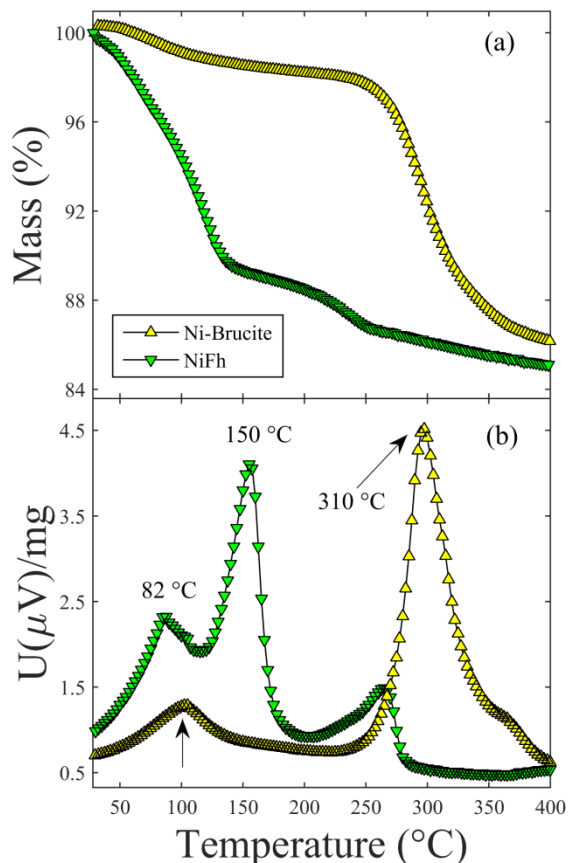
328 **Figure 7:** Mass (a) and DSC (b) of NiFh and Ni-hydroxide (Brucite) as a function of temperature. The drops in
329 the TGA correlates with the peaks observed in the DSC. The peak at 82 °C can be related to the H_2O present in
330 the intraparticle meso-space, while the peaks at 150 °C and 270 °C to interlayer H_2O. The Ni-brucite has a peak
331 at 100 °C and another at 310 °C that are related to H_2O desorption and Brucite degradation, respectively.

332 It has been argued that Ni-brucite coexists with the clay mineral particles and that this is pH
333 dependent(Michels et al., 2014). Although the TGA curves of NiFh and Ni-brucite are different, their
334 DSC diagrams show some similarity. For NiFh the endothermic peaks at 82 °C and 150 °C are
335 associated to different H_2O population that desorbs from the clay mineral, related to intraparticle and
336 interlayer H_2O losses, respectively. The peak at 100 °C for Ni-brucite may be related to H_2O
337 desorbing from the particle surface. These types of H_2O adsorbed in the clay minerals can be linked to
338 previous interpretations in the literature (Bordallo et al., 2008; Gates et al., 2012). The NiFh sample
339 and the Ni-brucite sample show peaks at around 260 °C and 320 °C respectively that can be attributed
340 to the degradation of Ni-brucite, since the Ni-brucite particles are either at the surface or confined

within the clay mineral pores, thus likely reducing the temperature threshold for this decomposition. It is well known that when smectites submitted to high temperatures, can have their structure modified in at least two ways: reduction of the layer charge or dehydroxylation. Layer charge reduction can be due to the migration of the interlayer cation into the octahedral sites, which has been observed in smectites saturated with small cations at temperatures as low as 125 °C(Skoubris et al., 2013), and it is known as Hofmann-Klemen effect(Komadel et al., 2005). Another type of known possible structure modification is the release at temperatures above 400 °C of the structural hydroxyl groups (OH) present in smectite layers(Green et al., 1970). However, it is important to notice that for the smectite clays studied in the present work the OH groups have been replaced by fluorine. This would imply that the DSC peak at 260 °C could also mean that the fluorine groups of the layer structure are being released.

In order to compare the dehydration of different NiFh samples, two isotherms with temperatures fixed at 70 °C and 150 °C (temperature of dehydration of the pre-heated samples) were measured in N_2 atmosphere. Both samples were prepared at room temperature at RH= 27 %, which are the same conditions used in the XRD experiments on non-preheated samples. The results are presented in Figure 8. In the asymptotic limit (125 min), for the sample heated at 70 °C the amount of mass lost is 8.7% while for the one heated at 150 °C the amount is 10.1%.
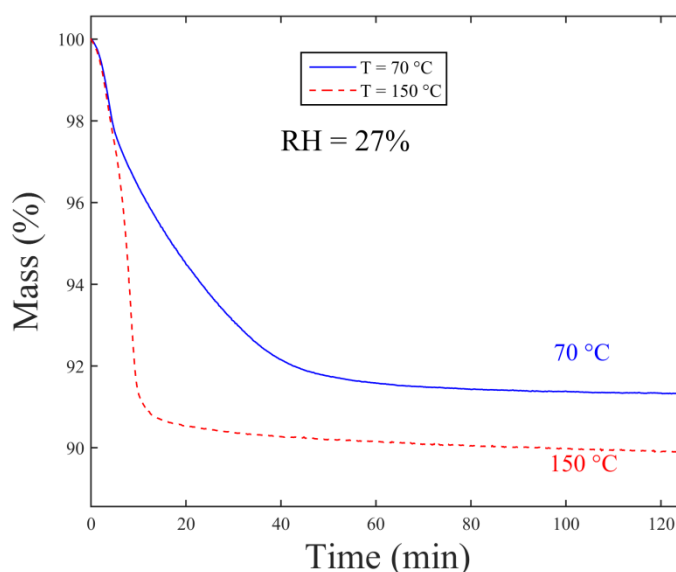
Figure 8: The amount of mass loss based on the isotherm at 70 °C and 150 °C.

3. Discussion

As described above, continuous peak shifts were found in the transition regions upon water uptake for this system. This can be related, to the existence of a Hendricks-Teller (HT) (da Silva et al.,

15

363 2002; Ferrage et al., 2007; Hendricks and Teller, 1942) type peak between two stable XRD peaks. In

364 such a case, the positions of the HT peaks can be directly related to the amount of different states in

365 the system. Simultaneously or alternatively, this continuous shift can be explained by different

366 geometrical arrangements of Ni^{2+}-H_2O complexes in the interlayers, such as the presence of Ni-

367 brucite $(Ni(OH)_2)$. Indeed Michels et al(Michels et al., 2014) reported that Ni-brucite was formed

368 during the cation exchange process from LiFh to NiFh due to the natural high pH of clay minerals in

369 solution, and it was shown that such structures may remain stable, which could possibly explain the

370 differences between dehydrated NiFh and LiFh or NaFh. Similar possibilities were also discussed by

371 Pitteloud et al.(Pitteloud et al., 2001), who found that Ni-montmorillonite at high hydration conditions

372 forms a complex structure of Ni^{2+}hexaaqua, which is very close to what is found for Ni^{2+} in aqueous

373 solution. Based on the results in Table 1, peak II can be label as 1WL. This is a stable hydration state

374 which is in agreement with Figure 3. Peak I, like the transitions peaks, may be related to one type of

375 confined Ni^{2+}-H_2O complex in which the free rotation of the H_2O molecule is limited. Furthermore,

376 peak III has an interlayer space corresponding to approximately 1.5 WL, which was also reported by

377 Tenorio et al. for LiFh(Tenorio et al., 2010). In sum all peaks I-IV may possibly be related to different

378 stable situations (coordination numbers and orientations of H_2O molecules) of Ni^{2+}-H_2O complexes in

379 the interlayers

380 The dependence of the XRD isotherms on the sample history is not clear (i.e. why there are

381 different XRD isotherm behaviors for the non-preheated and preheated samples). One explanation

382 might be a partial, but nevertheless minor, change in the layer structure initiated while heating the

383 samples at 150 °C. This has indeed been previously observed in smectites saturated with small-cations

384 at temperatures above 125 °C (Komadel et al., 2005; Skoubris et al., 2013).

385 From the TGA isotherm data at 150 °C the total mass loss is about 10.1%, and assuming that

386 this is only due to H_2O loss, this corresponds to approximately $33.7 \cdot 10^{20}$ H_2O molecules lost per gram

387 of NiFh. Considering that there are approximately 0.6 Ni^{2+} cations per unit cell of Fh (Kaviratna et

388 al., 1996) and that the number of unit cells per gram is the Avogadro's number divided by the molar

389 mass of the NiFh unit cell, one gets $7.71 \cdot 10^{20}$ unit cells per gram. Thus one gets approximately

390 $4.6 \cdot 10^{20}$ Ni^{2+} cations per gram of NiFh, and if one considers that all the lost H_2O is associated with

391 Ni^{2+} cations, the coordination number would be approximately 7.3 H_2O molecules per Ni^{2+}

392 (corresponding to 4.4 H_2O molecules per unit cell). Interestingly, this value is only slightly above the

393 Brucite structure coordination number, which is Ni^{2+} coordinated by 6 Oxygen atoms (Michels et al.,

394 2014). On the other hand, for the isotherm measured at 70 °C, 8.7% of the mass is lost during the

395 experiment, which corresponds to approximately 6.3 H_2O molecules per Ni^{2+}, using the same

396 calculation as above. This difference therefore amounts to about 1.0 H_2O molecules per Ni^{2+} cation

397 left in the sample, which is less than 1.4% of the total mass, assuming that all and only H_2O is lost at

398 150 °C. Consequently, the TGA measurements show that diffraction data were not collected in fully

399 dehydrated powders, indicating that the d_{001} value obtained using XRD does not directly represent the

400 amount of H_2O in the interlayer. Here it is important to point out that the detection limit of our XRD

401 measurements is about 1.5% (signal to noise ratio) which can be estimated from the ratio of the

402 dehydrated 0WL Bragg peak to the noise level in the 1WL peak position. Accordingly, if 1.5% of the

403 crystallites are in the monohydrated state they are "*invisible*" in the XRD experiments.

404

405 **4.   Conclusion**:

406   We have used XRD and TGA/DSC to study the intercalation of H_2O in the synthetic smectite

407 clay fluorohectorite with Ni^{2+} as interlayer cation using different sample preparation approaches, i.e.

408 pre-heated and non-pre-heated clays. XRD results show that the transition upon water adsorption from

409 the dehydrated state does not occur as an abrupt step, as commonly observed in other studies of

410 hydration in smectites, but shows a relatively continuous change. The latter might be linked to the

411 presence of various types of Ni^{2+}-H_2O complexes in the interlayers, such as Ni-brucite complexes or

412 Ni^{2+} hexaaqua and/or also to the coexistence with different hydration states within the scattering

413 volume. As reported in our recent work (Michels et al., 2014), Ni-brucite complexes can be present in

414 NiFh. If this behavior is common to smectite clays with transition metal cations, it will have

415 significant practical consequences in materials science and other areas where smectite clays are used.

416 The TGA/DSC results highlights further the effect of the initial conditions of the NiFh in hydration

417 experiments, suggesting that the sample pre-heated at 150 °C might have a reduced layer charge due

418 to the migration of Ni^{2+} to the layers (Hofmann-Klemen effect). This may explain the slightly

419 different H_2O adsorption isotherms obtained using XRD for the samples pre-heated at 150 °C and the

420 non-preheated samples.

421   Finally, via the Williamson-Hall analysis for four selected values of RH, the average particle

422 stack thickness and the average lattice strain were obtained. The former was found to be $Nd = 146 \pm$

423 11 nm for all studied samples in their stable hydration states, and to decrease when the system is in

424 transition between two hydration states. This observation may be attributed to an inhomogeneous

425 distribution of the intercalated H_2O within the clay interlayers. The lattice strain was found to be

426 proportional to the RH. This result indicates that the intercalation of H_2O in the basal planes cause

427 disorder in the stacking layers.

428   Future work would be to perform QENS experiments in order to fully quantify the H_2O

429 mobility (rotation and translation) within the interlayer space of the clay mineral and its relation to the

430 number of H_2O layers obtained in the present work. Through the analysis of the elastic incoherent

431 structure factor(Jacobsen et al., 2013), this technique might shed light on the identification of the

432 different Ni^{2+}-H_2O complexes, like Ni^{2+} hexaaqua and Ni-brucite, and their relation with the hydration

433 stability.

434

References:

Aguzzi, C., Cerezo, P., Sandri, G., Ferrari, F., Rossi, S., Bonferoni, C., Caramella, C., Viseras, C., 2014. Intercalation of tetracycline into layered clay mineral material for drug delivery purposes. Materials Technology 29, B96-B99.

Ayyappan, S., Subbanna, G.N., Gopalan, R.S., Rao, C.N.R., 1996. Nanoparticles of nickel and silver produced by the polyol reduction of the metal salts intercalated in montmorillonite. Solid State Ionics 84, 271-281.

Bergaya, F., Lagaly, G., 2013. Chapter 7.1 - Purification of Natural Clays, in: Faïza, B., Gerhard, L. (Eds.), Developments in Clay Science. Elsevier, pp. 213-221.

Bordallo, H.N., Aldridge, L.P., Churchman, G.J., Gates, W.P., Telling, M.T.F., Kiefer, K., Fouquet, P., Seydel, T., Kimber, S.A.J., 2008. Quasi-elastic neutron scattering studies on clay interlayer-space highlighting the effect of the cation in confined water dynamics. Journal of Physical Chemistry C 112, 13982-13991.

Chatterjee, A., Ebina, T., Onodera, Y., Mizukami, F., 2004. Effect of exchangeable cation on the swelling property of 2:1 dioctahedral smectite—A periodic first principle study. The Journal of Chemical Physics 120, 3414-3424.

Cummins, H.Z., 2007. Liquid, glass, gel: The phases of colloidal Laponite. Journal of Non-Crystalline Solids 353, 3891-3905.

da Silva, G.J., Fossum, J.O., DiMasi, E., Maloy, K.J., 2003. Hydration transitions in a nanolayered synthetic silicate: A synchrotron x-ray scattering study. Physical Review B 67.

da Silva, G.J., Fossum, J.O., DiMasi, E., Maloy, K.J., Lutnaes, S.B., 2002. Synchrotron x-ray scattering studies of water intercalation in a layered synthetic silicate. Physical Review E 66.

Dazas, B., Lanson, B., Breu, J., Robert, J.-L., Pelletier, M., Ferrage, E., 2013. Smectite fluorination and its impact on interlayer water content and structure: A way to fine tune the hydrophilicity of clay surfaces? Microporous and Mesoporous Materials 181, 233-247.

Dazas, B., Lanson, B., Delville, A., Robert, J.L., Komarneni, S., Michot, L.J., Ferrage, E., 2015. Influence of Tetrahedral Layer Charge on the Organization of Inter layer Water and Ions in Synthetic Na-Saturated Smectites. Journal of Physical Chemistry C 119, 4158-4172.

472 Ebrahimi, D., Whittle, A.J., Pellenq, R.J.-M., 2014. Mesoscale properties of clay aggregates
473 from potential of mean force representation of interactions between nanoplatelets. The
474 Journal of Chemical Physics 140, 154309.

475 Ferrage, E., Lanson, B., Michot, L.J., Robert, J.-L., 2010. Hydration Properties and Interlayer
476 Organization of Water and Ions in Synthetic Na-Smectite with Tetrahedral Layer Charge.
477 Part 1. Results from X-ray Diffraction Profile Modeling. Journal of Physical Chemistry C
478 114, 4515-4526.

479 Ferrage, E., Lanson, B., Sakharov, B.A., Drits, V.A., 2005. Investigation of smectite
480 hydration properties by modeling experimental X-ray diffraction patterns: Part I.
481 Montmorillonite hydration properties. American Mineralogist 90, 1358-1374.

482 Ferrage, E., Lanson, B., Sakharov, B.A., Geoffroy, N., Jacquot, E., Drits, V.A., 2007.
483 Investigation of dioctahedral smectite hydration properties by modeling of X-ray diffraction
484 profiles: Influence of layer charge and charge location. American Mineralogist 92, 1731-
485 1743.

486 Ferrage, E., Sakharov, B.A., Michot, L.J., Delville, A., Bauer, A., Lanson, B., Grangeon, S.,
487 Frapper, G., Jimenez-Ruiz, M., Cuello, G.J., 2011. Hydration Properties and Interlayer
488 Organization of Water and Ions in Synthetic Na-Smectite with Tetrahedral Layer Charge.
489 Part 2. Toward a Precise Coupling between Molecular Simulations and Diffraction Data.
490 Journal of Physical Chemistry C 115, 1867-1881.

491 Fleury, M., Kohler, E., Norrant, F., Gautier, S., M'Hamdi, J., Barre, L., 2013.
492 Characterization and Quantification of Water in Smectites with Low-Field NMR. Journal of
493 Physical Chemistry C 117, 4551-4560.

494 Gasparini, E., Tarantino, S.C., Ghigna, P., Riccardi, M.P., Cedillo-Gonzalez, E.I., Siligardi,
495 C., Zema, M., 2013. Thermal dehydroxylation of kaolinite under isothermal conditions.
496 Applied Clay Science 80-81, 417-425.

497 Gates, W.P., Bordallo, H.N., Aldridge, L.P., Seydel, T., Jacobsen, H., Marry, V., Churchman,
498 G.J., 2012. Neutron Time-of-Flight Quantification of Water Desorption Isotherms of
499 Montmorillonite. Journal of Physical Chemistry C 116, 5558-5570.

500 Giesting, P., Guggenheim, S., van Groos, A.F.K., Busch, A., 2012a. Interaction of carbon
501 dioxide with Na-exchanged montmorillonite at pressures to 640 bars: Implications for CO2
502 sequestration. International Journal of Greenhouse Gas Control 8, 73-81.

503 Giesting, P., Guggenheim, S., van Groos, A.F.K., Busch, A., 2012b. X-ray Diffraction Study
504 of K- and Ca-Exchanged Montmorillonites in CO2 Atmospheres. Environmental Science &
505 Technology 46, 5623-5630.

506 Grassi, G., Michels, L., Rozynek, Z., Altoe, M.A.S., dos Santos, E.C., da Fonseca, C.L.S.,
507 Droppa, R., Jr., Gholamipour-Shirazi, A., Fossum, J.O., da Silva, G.J., 2014. Cation
508 exchange dynamics confined in a synthetic clay mineral. European Physical Journal-Special
509 Topics 223, 1883-1893.

510 Green, J.M., Mackenzi.Kj, Sharp, J.H., 1970. Thermal reactions of synthetic hectorite. Clays
511 and Clay Minerals 18, 339-&.

Hansen, E.L., Hemmen, H., Fonseca, D.M., Coutant, C., Knudsen, K.D., Plivelic, T.S., Bonn, D., Fossum, J.O., 2012. Swelling transition of a clay induced by heating. Scientific Reports 2.

Hawkins, R.K., Egelstaff, P.A., 1980. Interfacial water-structure in montmorillonite from neutron-diffraction experiments. Clays and Clay Minerals 28, 19-28.

Hemmen, H., Alme, L.R., Fossum, J.O., Meheust, Y., 2010. X-ray studies of interlayer water absorption and mesoporous water transport in a weakly hydrated clay. Physical Review E 82.

Hemmen, H., Rolseth, E.G., Fonseca, D.M., Hansen, E.L., Fossum, J.O., Pivelic, T.S., 2012. X-ray Studies of Carbon Dioxide Intercalation in Na-Fluorohectorite Clay at Near-Ambient Conditions. Langmuir 28, 1678-1682.

Hendricks, S., Teller, E., 1942. X-Ray Interference in Partially Ordered Layer Lattices. The Journal of Chemical Physics 10, 147-167.

Israelachvili, J.N., 2011. 4 - Interactions Involving Polar Molecules, in: Israelachvili, J.N. (Ed.), Intermolecular and Surface Forces (Third Edition). Academic Press, San Diego, pp. 71-90.

Jacobsen, J., Rodrigues, M.S., Telling, M.T.F., Beraldo, A.L., Santos, S.F., Aldridge, L.P., Bordallo, H.N., 2013. Nano-scale hydrogen-bond network improves the durability of greener cements. Scientific Reports 3.

Kaviratna, P.D., Pinnavaia, T.J., Schroeder, P.A., 1996. Dielectric properties of smectite clays. Journal of Physics and Chemistry of Solids 57, 1897-1906.

Komadel, P., Madejova, J., Bujdak, J., 2005. Preparation and properties of reduced-charge smectites - A review. Clays and Clay Minerals 53, 313-334.

Malikova, N., Cadene, A., Dubois, E., Marry, V., Durand-Vidal, S., Turq, P., Breu, J., Longeville, S., Zanotti, J.M., 2007. Water diffusion in a synthetic hectorite clay studied by quasi-elastic neutron scattering. Journal of Physical Chemistry C 111, 17603-17611.

Malikova, N., Cadène, A., Marry, V., Dubois, E., Turq, P., 2006. Diffusion of Water in Clays on the Microscopic Scale: Modeling and Experiment. The Journal of Physical Chemistry B 110, 3206-3214.

Michels, L., Fossum, J.O., Rozynek, Z., Hemmen, H., Rustenberg, K., Sobas, P.A., Kalantzopoulos, G.N., Knudsen, K.D., Janek, M., Plivelic, T.S., da Silva, G.J., 2015. Intercalation and Retention of Carbon Dioxide in a Smectite Clay promoted by Interlayer Cations. Sci. Rep. 5.

Michels, L., Ribeiro, L., Pedrosa Mundim, M.S., Sousa, M.H., Droppa, R., Jr., Fossum, J.O., da Silva, G.J., Mundim, K.C., 2014. EXAFS and XRD studies in synthetic Ni-fluorohectorite. Applied Clay Science 96, 60-66.

Mitra, S., Prabhudesai, S.A., Chakrabarty, D., Sharma, V.K., Vicente, M.A., Embs, J.P., Mukhopadhyay, R., 2013. Dynamics of water in synthetic saponite clays: Effect of trivalent ion substitution. Physical Review E 87.

549 Morrow, C.P., Yazaydin, A.O., Krishnan, M., Bowers, G.M., Kalinichev, A.G., Kirkpatrick,
550 R.J., 2013. Structure, Energetics, and Dynamics of Smectite Clay Interlayer Hydration:
551 Molecular Dynamics and Metadynamics Investigation of Na-Hectorite. Journal of Physical
552 Chemistry C 117, 5172-5187.

553 Oueslati, W., Ben Rhaiem, H., Amara, A.B., 2011. XRD investigations of hydrated
554 homoionic montmorillonite saturated by several heavy metal cations. Desalination 271, 139-
555 149.

556 Pascual, C.M., Argueelles, A., Leoni, M., Khainakov, S.A., Blanco, J.A., 2014. Location of
557 Ni2+ in nickel-intercalated vermiculites. Applied Clay Science 91-92, 79-86.

558 Pitteloud, C., Powell, D.H., Fischer, H.E., 2001. The hydration structure of the Ni(2+) ion
559 intercalated in montmorillonite clay: a neutron diffraction with isotopic substitution study.
560 Physical Chemistry Chemical Physics 3, 5567-5574.

561 Schaef, H.T., Ilton, E.S., Qafoku, O., Martin, P.F., Felmy, A.R., Rosso, K.M., 2012. In situ
562 XRD study of Ca2+ saturated montmorillonite (STX-1) exposed to anhydrous and wet
563 supercritical carbon dioxide. International Journal of Greenhouse Gas Control 6, 220-229.

564 Sellin, P., Leupin, O.X., 2013. The use of clay as an engineered barrier in radioactive-waste
565 management - a review. Clays and Clay Minerals 61, 477-498.

566 Skipper, N.T., Refson, K., McConnell, J.D.C., 1991a. Computer simulation of interlayer
567 water in 2:1 clays. The Journal of Chemical Physics 94, 7434-7445.

568 Skipper, N.T., Soper, A.K., McConnell, J.D.C., 1991b. The structure of interlayer water in
569 vermiculite. Journal of Chemical Physics 94, 5751-5760.

570 Skipper, N.T., Soper, A.K., Smalley, M.V., 1994. Neutron-diffraction study of calcium
571 vermiculite - hydration of calcium-ions in a confined environment. Journal of Physical
572 Chemistry 98, 942-945.

573 Skoubris, E.N., Chryssikos, G.D., Christidis, G.E., Gionis, V., 2013. Structural
574 characterization of reduced-charge montmorillonites. Evidence based on ftir spectroscopy,
575 thermal behavior, and layer-charge systematics. Clays and Clay Minerals 61, 83-97.

576 Sposito, G., Skipper, N.T., Sutton, R., Park, S.H., Soper, A.K., Greathouse, J.A., 1999.
577 Surface geochemistry of the clay minerals. Proceedings of the National Academy of Sciences
578 of the United States of America 96, 3358-3364.

579 Tambach, T.J., Hensen, E.J.M., Smit, B., 2004. Molecular simulations of swelling clay
580 minerals. Journal of Physical Chemistry B 108, 7586-7596.

581 Tamura, K., Yamada, H., Nakazawa, H., 2000. Stepwise hydration of high-quality synthetic
582 smectite with various cations. Clays and Clay Minerals 48, 400-404.

583 Tenorio, R.P., Alme, L.R., Engelsberg, M., Fossum, J.O., Hallwass, F., 2008. Geometry and
584 dynamics of intercalated water in Na-fluorhectorite clay hydrates. Journal of Physical
585 Chemistry C 112, 575-580.

586 Tenorio, R.P., Engelsberg, M., Fossum, J.O., da Silva, G.J., 2010. Intercalated Water in
587 Synthetic Fluorhectorite Clay. Langmuir 26, 9703-9709.

588 Wertheim, G.K., Butler, M.A., West, K.W., Buchanan, D.N.E., 1974. Determination of the
589 Gaussian and Lorentzian content of experimental line shapes. Review of Scientific
590 Instruments 45, 1369-1371.

591 Zheng, Y., Zaoui, A., 2011. How water and counterions diffuse into the hydrated
592 montmorillonite. Solid State Ionics 203, 80-85.

593 Zheng, Y., Zaoui, A., Shahrour, I., 2010. Evolution of the interlayer space of hydrated
594 montmorillonite as a function of temperature. American Mineralogist 95, 1493-1499.

595 Zhou, J.H., Boek, E.S., Zhu, J.X., Lu, X.C., Sprik, M., He, H.P., 2015. Molecular Simulation
596 Study of Hydrated Na-Rectorite. Langmuir 31, 2008-2013.

597

598